NSU3D Results for the Second AIAA High Lift Prediction Workshop

Dimitri Mavriplis *
Michael Long †
Troy Lake ‡
Department of Mechanical Engineering
University of Wyoming, Laramie, Wyoming, USA
Marc Langlois §
Advanced Aerodynamics
Bombardier Aerospace, Montréal, Québec, Canada

Simulation results for the second AIAA CFD High Lift Prediction Workshop using the unstructured computational fluid dynamics code NSU3D are presented. The solution algorithms employed in NSU3D for this study are described along with examples of convergence history and computational cost. The geometry used for the simulation consists of the DLR-F11 wing-body with high-lift system deployed in a landing configuration. This geometry is representative of a modern transport aircraft high-lift system that has been tested experimentally over a suitable Reynolds number range. Results are presented from two sets of computational studies, the first performed at the University of Wyoming using standard workshop unstructured meshes, and the second performed at Bombardier Aerospace using in-house generated meshes. In both cases, results are presented for two different turbulence models, allowing an assessment of the sensitivity of the results to grid densities, grid types, and turbulence models. Results consist of computed force and moment coefficients across a range of angles of attack and for two different Reynolds numbers, as well as surface pressure profiles and off-body velocity profiles, all of which are compared with experimental data. The results compare favorably with experimental data and generally fall within the standard deviation of the workshop collective results. Computations using the Spalart-Allmaras turbulence model tend to overpredict the maximum lift value and incidence, while results using the k-omega model tend to underpredict the maximum lift value. The best agreement in terms of force coefficients is observed with the k-omega turbulence model using the Bombardier internally generated meshes.

I. Introduction

The stated goals of the High-Lift Prediction Workshop (HLPW) series are to assess the state-of-the-art in computational fluid dynamics (CFD) methods for simulation of high lift-configurations and to provide a forum for exchange of ideas and practices related to this class of problems.[1] The second High-Lift Prediction Workshop was sponsored by the AIAA Applied Aerodynamics Technical Committee and was held prior to the 21st AIAA CFD conference in San Diego CA in June 2013.[2,3] Building on the success of the first workshop held in the summer of 2010,[1] the second workshop focused on a more representative configuration for modern transport aircraft design for which extensive experimental data is available. The chosen configuration consists of the DLR F11 high-lift configuration, which was the subject of the previous European High Lift Programme

*Professor, Associate Fellow, email: mavripl@uwyo.edu
†Applications Engineer, Member, email: mlong16@uwyo.edu
‡Graduate Student, Member AIAA , email: tlake4@uwyo.edu
§Senior Engineering Specialist, email: marc.h.langlois@aero.bombardier.com

(EUROLIFT).[4] The DLR-F11 is a wing-body configuration with a wing of aspect ratio 9.353 with a quarter-chord sweep angle of 30 degrees and a 4 degree dihedral angle. The high-lift system consists of a full span leading-edge slat and single-slotted trailing-edge flap. A slat deflection of 26.5 degrees and a flap deflection of 32 degrees are specified for the workshop test cases. As part of the EUROLIFT program, a half-span model was tested at various Reynolds numbers and incidences[5] as depicted in Figure 1. In addition to force and moment data, high quality surface pressure data were recorded, as well as off-body field velocity data using PIV measurement techniques.

Due to the geometric complexity of the model, three workshop test cases of increasing geometric complexity were conceived. Case 1 consists of a simple clean wing-slat-flap system with no fairings, supports or brackets, while for Case 2, the slat brackets and flap-track fairings are added to the geometry for higher fidelity, as shown in Figure 2. Case 3 includes additional geometry components designed to simulate the pressure tube bundles used in the wind-tunnel model, which were found to have an influence on overall experimental measurements during the test campaign.[6]

This paper documents the results obtained for the workshop using the NSU3D unstructured mesh Reynolds-averaged Navier-Stokes (RANS) solver. The NSU3D code has been a participant in the first high-lift prediction workshop,[7] the first aeroelastic prediction workshop,[8] and has been present in all five Drag Prediction workshops since 2001.[9–15] The results presented in this paper were obtained in two separate computational studies, the first one performed at the University of Wyoming, and the second one performed at Bombardier Aerospace. The former study relied on a series of unstructured meshes which were generated jointly at the University of Wyoming and at Cessna Aircraft, and which have been made available as standard (Series D) workshop meshes.[2] The latter study relied exclusively on internally generated meshes using standard company "best-practices" in order to assess the standard workflow process within Bombardier Aerospace for high-lift analysis. In both cases, coarse, medium and fine resolution meshes were generated and used, and results using two different turbulence models were obtained. Thus, the current study enables the examination of the sensitivity of high-lift computational results obtained with the NSU3D code to mesh resolution, mesh type, and turbulence models.

From the collective workshop results it has been determined that the slat brackets and flap track fairings play a critical role in the stall mechanism of this high-lift configuration with the result that the geometry simplifications used in Case 1 compromised the ability of the simulations to predict the maximum lift point.[3] However, the approximate geometry of Case 1 considerably simplifies the mesh generation process. Therefore, for the purposes of this work, Case 1 is treated principally as a mesh convergence study. The majority of the current study is focused on Case 2, for which reasonably fine meshes could be generated and which includes sufficient geometric detail to reproduce the appropriate stall mechanism. Case 3 was not attempted in this work, due to the added geometric complexity and the secondary nature of the influence of the pressure tube bundles on the aerodynamic performance of the model.

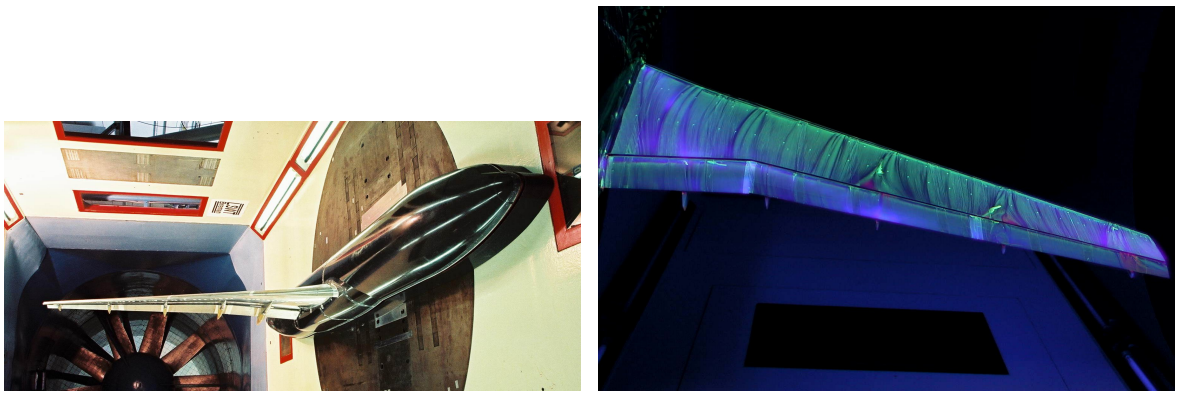

Figure 1. DLR-F11 Wind tunnel model and sample surface oil flow pattern

In the next section, the meshes used in the current study are described. This is followed with a brief description of the NSU3D unstructured mesh discretization and solver, including an overview of convergence characteristics observed for the workshop cases. Results in terms of forces, moments, surface pressures, and field velocity profiles are detailed in the Results section, where computational results are compared to assess the effect of grid resolution, grid type, and turbulence model selection, and agreement with experimental

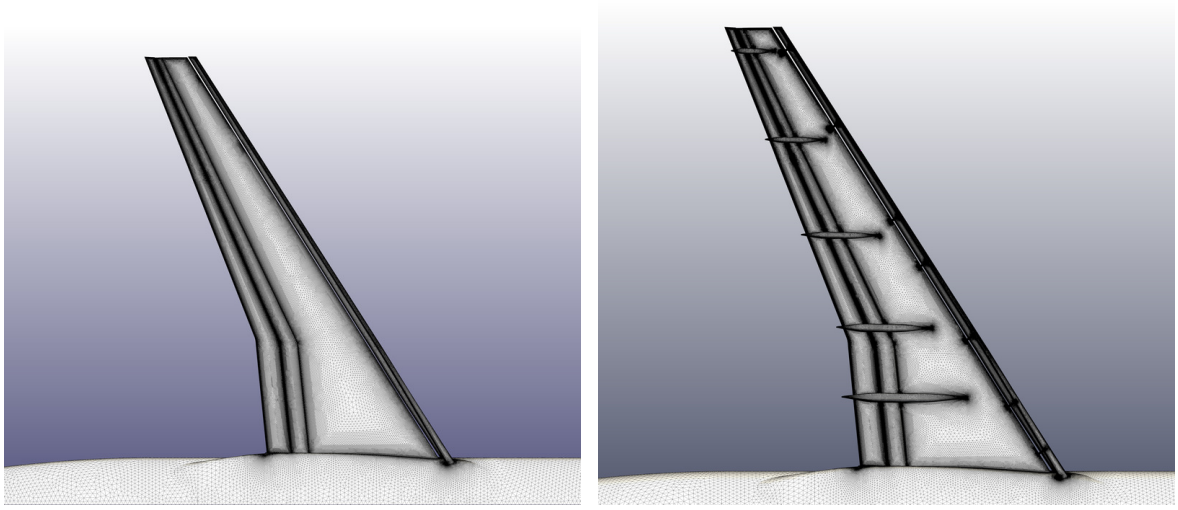

(a) Case 1 geometry (b) Case 2 geometry

Figure 2. Medium resolution VGRID generated workshop mesh for Case1 and Case 2 showing geometric simplification in Case 1

.

data is discussed. The paper concludes with a discussion of possible future work for advancing the predictive capabilities of high-lift computations.

II. Grid Generation

The high-lift prediction workshop series adheres to a set of standard gridding guidelines that have been developed and promoted over the years through the Drag Prediction Workshop (DPW) series[16] and the first High-Lift workshop.[1] The meshing guidelines include a far field boundary at 100 chord lengths away, a normal spacing at the wall of $y^+ = 1.0$ for the coarsest grids, with progressively smaller spacings on the finer grids, chordwise spacings at the element leading and trailing edges of approximately 0.1% chord on the coarse mesh, and spanwise spacings of 0.1% at the element root and tip on the coarsest mesh as well. The overall size of the grids is targeted to grow by a factor of three when going from coarse to medium, and medium to fine. Care is taken to generate corresponding coarse, medium and fine meshes with self-similar resolution distributions, such that these grids can be considered to be of the same "family" for grid convergence studies. The medium grid is specified to be representative of the resolution level used in current industrial production runs, although no specific node or cell counts are specified for any of these grid levels.[3]

Two sets of grids are used in the present study. The first set was generated by the second author in collaboration with Mark Chaffin of Cessna Aircraft using the VGRID software package.[17] VGRID is an advancing-layer unstructured mesh generator that produces fully tetrahedral meshes. Triplets of highly stretched tetrahedra in boundary layer regions are merged into prisms in a postprocessing operation, resulting in a mixed prismatic-tetrahedral mesh with a small number of pyramidal elements at prismatic-tetrahedral interfaces. These meshes are available in tetrahedral or mixed-element form as standard workshop meshes and are labeled as the "D" series of meshes on the workshop web site.[2] A total of five meshes were generated: a sequence of coarse, medium and fine meshes for Case 1, and medium resolution meshes for Case 2, and Case 3, although the Case 3 mesh was not used in the present study.

The second set of meshes was generated internally at Bombardier Aerospace using their established "best practices" for high-lift aerodynamic analysis. These meshes were constructed using the Ansys ICEM-Tetra/Prism mesh generator.[18] This approach is based on an octree subdivision of the computational domain, that intersects the geometry surface. Thus, the surface grid is obtained as a result of the interior mesh subdivision process and contains mostly isotropic triangles, as opposed to the spanwise stretching that is typically used in the VGRID process. Curvature-based refinement is also available to cluster surface mesh points in regions of interest. Prismatic layers are inserted into the volume mesh in a second pass by growing

layers from the surface triangulation based on inputs that are used to control the spacing and growth rate of the layers in boundary layer regions. A total of four meshes were generated in this manner, a sequence of coarse, medium and fine meshes for Case 1, and a medium resolution mesh for Case 2.

Tables 1 and 2 describe the characteristics of these meshes, were it can be seen that the two sets of meshes have similar resolution, although the ICEM meshes have slightly higher total node counts. A global view of the Case 1 coarse, medium and fine mesh sequences is shown in Figure 3 and Figure 4 for the VGRID and ICEM meshes, respectively. Although the global resolutions are similar, the ICEM meshes have a slower growth rate in the boundary layer leading to a larger ratio of prisms to tetrahedra. Additionally, the relative distribution of resolution in the two sets of meshes can be quite different in various regions of the computational domain, largely due to the different mesh construction approaches, as illustrated in Figure 5 and 6 for the Case 2 meshes. One notable difference is that the ICEM meshes contain more spanwise resolution due to the isotropic nature of the surface triangulations. Figure 7 depicts the surface y^+ values for the Case 2 meshes generated by both approaches for the high-Reynolds number (15 million) Case 2b test case at 16 degrees incidence. As can be seen from the figures, the tight normal spacing at the wall in these meshes achieves values of $y^+ < 1$ over most of the surface geometry. These meshes were designed for the high-Reynolds number case (Case 2b) and were also used for the lower Reynolds number case (Case 2a) where the Reynolds number was 1.35 million.

Table 1. Characteristics of VGRID generated workshop meshes.

Grid Name	Nodes	Tetras	Prisms	First Cell Height	VGRID Growth Rate and Factor
Case 1 (Coarse)	10,229,072	13,820,586	15,395,027	5.5 e-04	1.15 - 0.02
Case 1 (Medium)	30,767,679	58,300,006	40,864,715	3.7 e-04	1.15 - 0.02
Case 1 (Fine)	75,978,568	186,999,490	86,668,878	3.7 e-04	1.15 - 0.02
Case 2	41,511,973	71,418,665	57,565,283	3.7 e-04	1.15 - 0.02

Table 2. Characteristics of ICEM-TETRA generated meshes.

Grid Name	Nodes	Tetras	Prisms	First Cell Height	Growth Ratio
Case 1 (Coarse)	17,477,000	10,083,000	30,953,000	5.5 e-04	1.085 - 1.8
Case 1 (Medium)	43,859,000	25,542,000	77,016,000	3.5 e-04	1.085 - 1.8
Case 1 (Fine)	121,407,000	85,978,000	208,056,000	2.4 e-04	1.085 - 1.8
Case 2	49,018,000	28,356,000	86,120,000	3.5 e-04	1.085 - 1.8

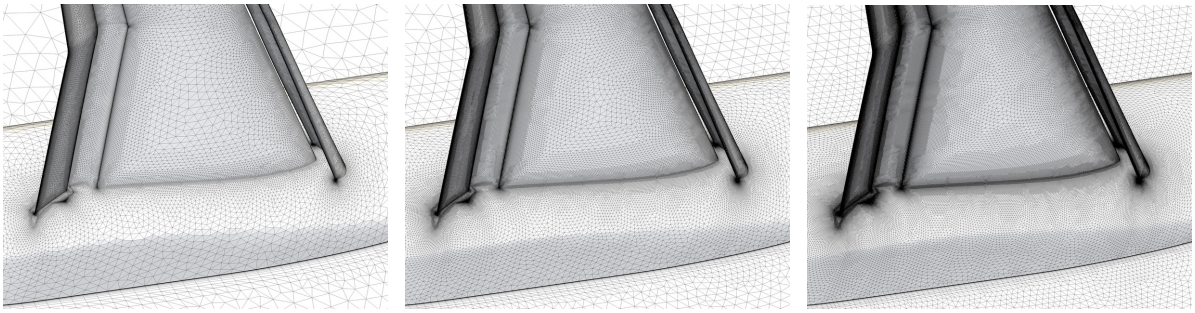

(a) Coarse (b) Medium (c) Fine

Figure 3. Sequence of meshes generated using VGRID for Case 1 grid refinement study

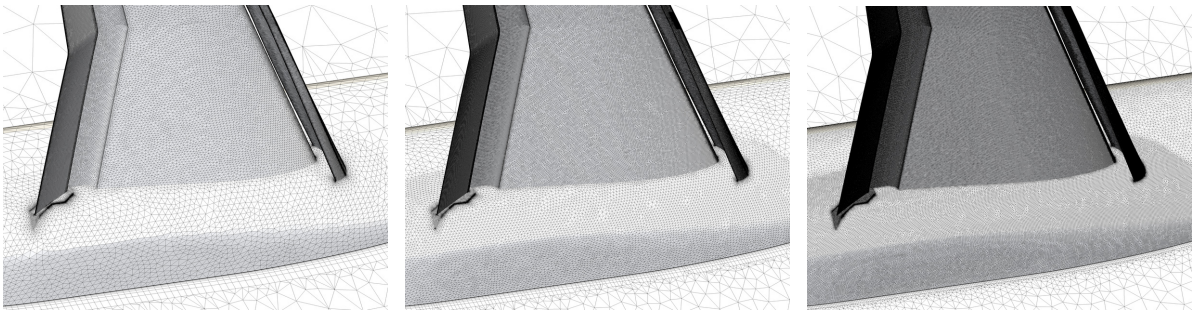

(a) Coarse (b) Medium (c) Fine

Figure 4. Sequence of meshes generated using ICEM-Tetra for Case 1 grid refinement study

III. Solver Description

The NSU3D code is an unstructured mesh multigrid Reynolds-averaged Navier-Stokes (RANS) solver for high-Reynolds number external aerodynamic applications. The NSU3D discretization employs a vertex-based approach, where the unknown fluid and turbulence variables are stored at the vertices of the mesh, and fluxes are computed on faces delimiting dual control volumes, with each dual face being associated with a mesh edge. This discretization operates on hybrid mixed-element meshes, generally employing prismatic elements in highly stretched boundary layer regions, and tetrahedral elements in isotropic regions of the mesh away from the aircraft surfaces. A single edge-based data-structure is used to compute flux balances across all types of elements. The convective terms are discretized as central differences with added matrix dissipation. Second-order accuracy is achieved by formulating these dissipative terms as an undivided bi-harmonic operator, which is constructed in two passes of a nearest-neighbor Laplacian operator. In the matrix form, this dissipation is similar to that produced by a Riemann solver gradient-based reconstruction scheme, and is obtained by replacing the difference in the reconstructed states on each side of the control volume interface by the undivided differences along mesh edges resulting from the biharmonic operator construction. These differences are then multiplied by the characteristic matrix to obtain the final dissipation terms. A Roe upwind scheme using least-squares gradient reconstruction is also available in the NSU3D solver, although this option has not been used in the present study. Previous work has shown that the matrix dissipation and Roe schemes in NSU3D give very similar results, with the matrix dissipation scheme being slightly less diffusive overall.[14,19]

The baseline NSU3D discretization employs a finite-difference scheme to approximate the thin-layer form of the viscous terms for the Navier-Stokes equations, although this is done in a multidimensional fashion, by computing a Laplacian of the velocity field.[20] The main approximation in this approach is the omission of the cross-derivative viscous terms, and the assumption of a locally constant viscosity. The discretization of the full Navier-Stokes terms has also been implemented using a two-pass edge-based loop approach,[14] although this option has not been used in the present study.

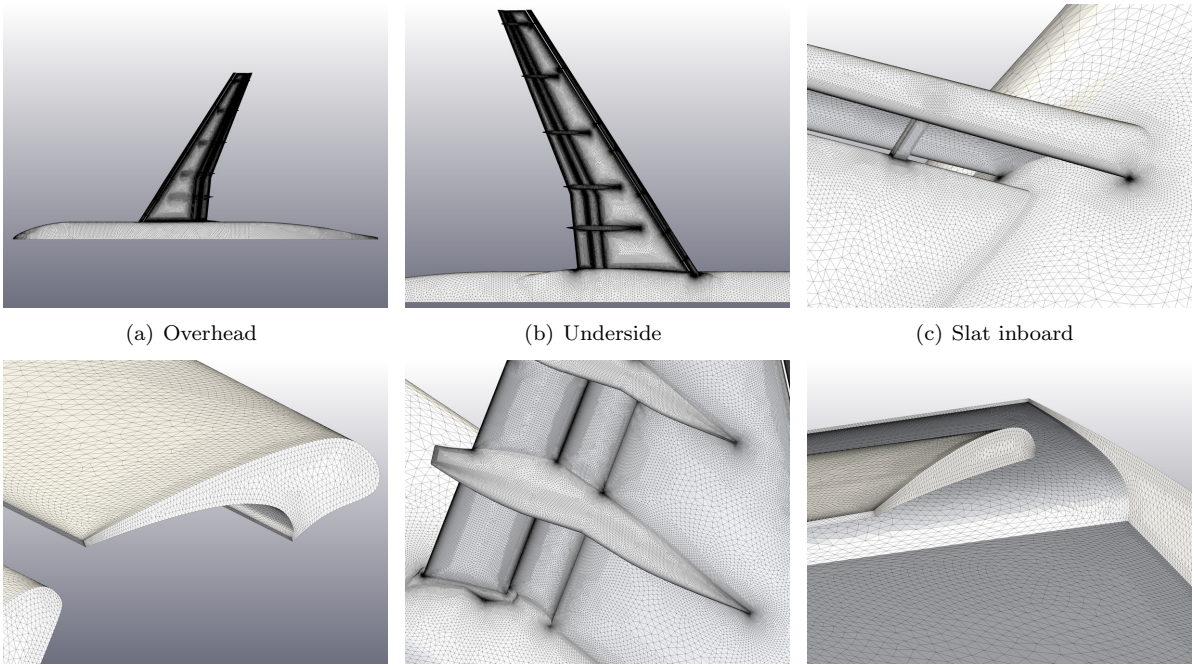

(a) Overhead (b) Underside (c) Slat inboard

(d) Slat outboard (e) Flap inboard (f) Flap outboard

Figure 5. Mesh resolution details for 41.5 million point mesh generated using VGRID for Case 2 study

.

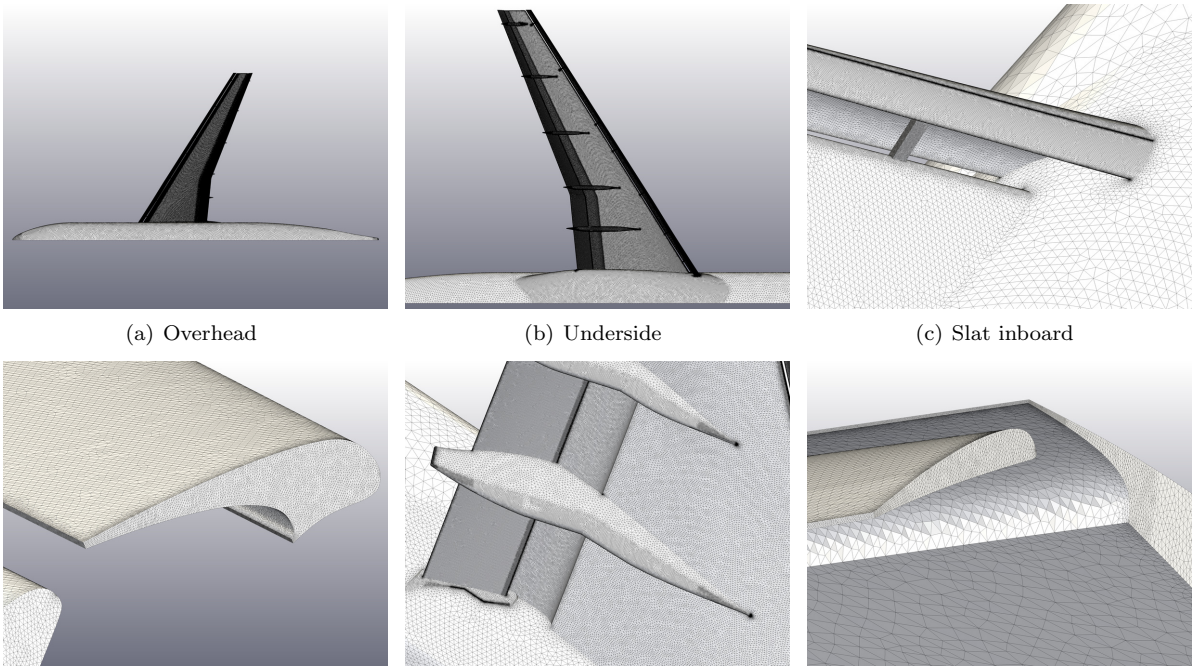

(a) Overhead (b) Underside (c) Slat inboard

(d) Slat outboard (e) Flap inboard (f) Flap outboard

Figure 6. Mesh resolution details for 49.0 million point mesh generated using ICEM-Tetra for Case 2 study

.

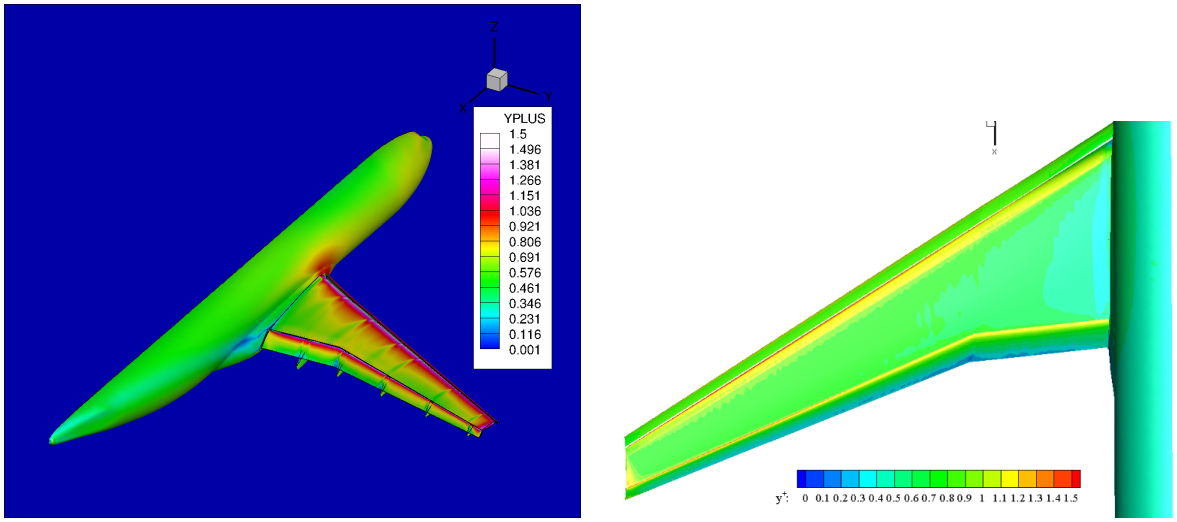

(a) Vgrid mesh

(b) ICEM mesh

Figure 7. Distribution of y^+ on medium mesh for VGRID and ICEM-Tetra generated meshes at Reynolds number of 15.1 million

.

NSU3D incorporates the single equation Spalart-Allmaras turbulence model,[21] as well as a standard $k-\omega$ two-equation turbulence model,[22] and the two-equation shear-stress transport (SST) model due to Menter.[23] Facilities for specified transition location based on the surface geometry are provided.

The basic time-stepping scheme in NSU3D consists of a three stage explicit multistage scheme. Convergence is accelerated by a local block-Jacobi preconditioner in regions of isotropic grid cells. In boundary layer regions, where the grid is highly stretched, a line preconditioner is employed to relieve the stiffness associated with the mesh anisotropy.[24] An agglomeration multigrid algorithm is used to further enhance convergence to steady-state.[20,25] The Jacobi and line preconditioners are used to drive the various levels of the multigrid sequence, resulting in a rapidly converging solution technique. A preconditioned GMRES-based Newton-Krylov solver is also available, where a linear version of the multigrid scheme is used as a preconditioner for the GMRES solver.[26]

NSU3D employs a dual level parallelization strategy invoking the MPI interface for interprocessor communication across distributed memory nodes, with the ability to use OpenMP constructs for inter-node shared memory parallelism. In general, the code is run in MPI-only mode since hybrid MPI-OpenMP has only been found to be advantageous on specialized hardware. NSU3D has been shown to scale well on massively parallel computer architectures using up to 32,786 cores, as shown in Figure 8.

For the purposes of this study, the matrix-based artificial dissipation discretization and multidimensional thin-layer viscous term formulation were used exclusively. Results were obtained using both the Spalart-Allmaras and k-omega turbulence models, and all runs were performed in a fully turbulent mode (no transition specification).

A typical convergence history for Case 2b is shown in Figure 9. For this particular case, the angle of attack is 16 degrees, and the computation is performed on the workshop D-series configuration 4 standard resolution grid, which contains 41.5 million points, with 57 million prismatic elements and 71 million tetrahedral elements, as described in Table 1.

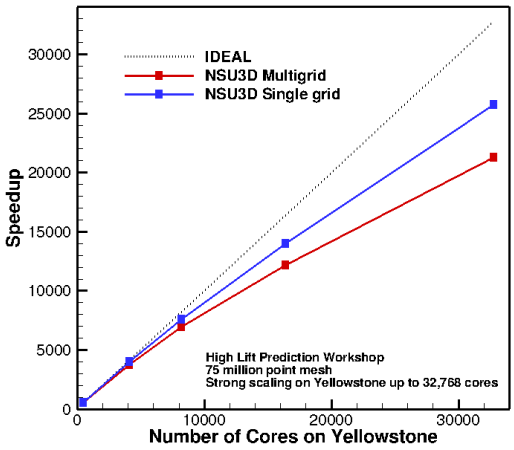

Figure 8. Scalability of multigrid solver in NSU3D using up to 32,786 cores for Case 1 fine level mesh

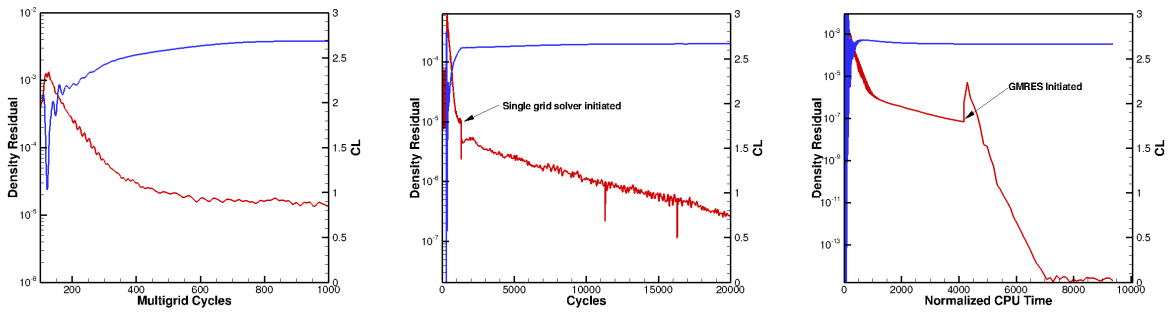

(a) Initial multigrid convergence

(b) Further convergence using single grid algorithm

(c) Complete convergence using GMRES algorithm

Figure 9. Convergence histories using various solver techniques for Case 2b at 16 degrees incidence on 41.5 million point VGRID mesh

In general, the multigrid algorithm using 4 levels converges 3 to 4 orders of magnitude over 1000 cycles. At this point, the force coefficients are converged to engineering accuracy in most cases. However, the residual convergence stalls and considerable additional effort can be required to converge the residuals further. For the Bombardier results, the multigrid solver was run for approximately 1000 to 2000 iterations at which point the force coefficients were considered sufficiently converged. For the University of Wyoming results, additional effort was expended to obtain tighter final convergence tolerances. This was achieved by switching to a single grid solver after 1000 multigrid cycles and running the solver out for up to 20,000 iterations until the residual was decreased by another several orders of magnitude and less than 1 count variation in the force coefficients was achieved. This was possible for most of the cases reported in this study, although some cases near stall required longer run times than others. The GMRES solver was also invoked on one case to examine the possibility of converging these cases to machine zero. Figure 9 also depicts the convergence history for the same case at 16 degrees where the multigrid preconditioned GMRES solver was invoked after an initial convergence run using the multigrid solver as a linear solver.[26] As seen from the figure, the GMRES algorithm is successful in driving the residuals to machine zero relatively quickly. While this convergence history is far from optimal, it demonstrates the possibility of driving the residuals to zero for difficult problems where the standard multigrid algorithm stalls.

IV. Case 1 - Grid Convergence Study

The first test case required for the workshop is a grid convergence study using the three successively refined grids for Configuration 1 described in the previous section. The test conditions for this case are specified as:

- Mach Number = 0.175
- Angle-of-attack = 7° and 16°
- Reynolds Number = 15.1 million based on mean aerodynamic chord (MAC)

The grid convergence plots are made versus the grid index, defined as the inverse of the number of grid points to the 2/3 power, with the understanding that for a family of self-similar coarse to fine grids, this quantity should be representative of the average cell size h to the second power. Thus, straight-line plots in these figures are indicative of second-order accurate spatial convergence and extrapolation to the y-axis provides an estimate of the values which would be predicted in the presence of infinite grid resolution.

Figure 10 shows the grid convergence behavior of the lift, drag and moment coefficients for the 7° and 16° incidence cases. Results are shown using the first set of grids (generated using VGRID) for both turbulence models (Spalart-Allmaras and k-omega), and using the second set of grids (generated using ICEM-Tetra) for the k-omega model only. For these cases, the lift, drag and moment coefficients exhibit close to linear convergence, although the moment coefficient variation at the higher incidence is slightly less regular than the others. In general, reasonable grid convergence can be deduced from these plots, although the inclusion of additionally fine meshes would help to support this statement. On the other hand, we note that the fine grids are in the range of 100 million points, making additional levels of grid refinement a challenging exercise.

Figures 11 and 12 provide an illustration of the sensitivity of the computed surface pressure coefficients at two representative span locations (second inboard and outermost span locations) with respect to grid resolution, for both angles of attack and both turbulence models. Overall, relatively little change in the computed surface pressure coefficients is observed between the coarse, medium and fine mesh levels, particularly for the lower angle of attack case. The highest discrepancies are observed for the outboard station in the 16 degree case, and there is somewhat more variation for the k-omega turbulence model results than for the Spalart-Allmaras model results, although in both cases the medium and fine grid results compare well.

A full set of velocity profile plots is given for both angles of attack and both turbulence models in Figures 13 through 16. Similarly to the pressure plots, these figures are intended to illustrate the effect of grid refinement on computational results, and therefore experimental data is not included. The trends are similar to those observed for the pressure comparison. The variation in the velocity profiles for the 7 degree case show relatively small differences particularly between the medium and fine mesh levels at almost all locations. For the 16 degree case, larger differences are observed, particularly for the k-omega model at the downstream and outboard profile locations. Nevertheless, the observed variations of the velocity profiles with increasing grid resolution may be misleading, since entire flow features such as wakes from upstream components are missing in some cases and it is postulated that significant increases in grid resolution that may be beyond current capabilities will be required to fully resolve all such features.

V. Case 2a - Low Reynolds Number Alpha Sweep

The second case for the workshop is based on the more realistic geometry that includes the slat brackets and flap track fairings. Case 2a involves an angle of attack sweep at a Mach number of 0.175 and a Reynolds number of 1.35 million. The specified incidence values from the workshop test case are 0^o, 7^o, 12^o, 16^o, 18.5^o, 19^o, 20^o, 21^o, although additional incidences have been run near the maximum lift point to obtain a more accurate lift curve. Computations using both turbulence models were performed on the VGRID mesh for this case, although only the k-omega turbulence model was used for the Bombardier calculations on the ICEM mesh. Both meshes require roughly equivalent computational effort, with the VGRID mesh containing 41.5 million points, and the ICEM mesh 49 million points.

Figure 17 contains the computed lift and drag coefficients plotted as a function of angle of attack, as well as a drag polar and pitching moment plot. The computed lift and drag values agree well with experimental data in the linear region of the lift curve. However, the Spalart-Allmaras results (on the VGRID mesh) overpredict the maximum lift value and angle of attack, while the k-omega results on the same mesh underpredict these

values. The k-omega model results on the ICEM mesh agree best with the experimental data right up to the maximum lift point, although additional calculations at higher angles of attack will be required to determine the stall characteristic in this case. The Spalart-Allmaras model lift curve breaks at 20 degrees, while the k-omega results on the same mesh break at 18.5 degrees, again bracketing the $C_{L_{MAX}}$ incidence of the experimental results. The anomalous behavior of the k-omega lift values on the VGRID mesh around 20 degrees were verified by filling in the lift curve with additional calculations at 19 and 20.5 degrees. When plotted in drag polar form, the $C_{L_{MAX}}$ point occurs approximately at the same location for both models in terms of drag. Plotting drag as a function of angle of attack, it is seen that drag is slightly overpredicted for 16 degrees and higher incidences. However the drag predicted by the Spalart-Allmaras model on the VGRID mesh and the k-omega model on the ICEM mesh agree closely right up to 18.5 degrees. The k-omega results on the VGRID mesh tend to overpredict drag at the higher incidences, which is not surprising given the early stall behavior of these runs. The pitching moment is slightly over predicted (in absolute value) at lower incidences by all models, although the k-omega model on the VGRID mesh provides the closest agreement with experimental data at the higher angles of attack including beyond stall.

A selected set of computed surface pressure plots for this case is shown in Figures 18 through 21. Results are given at four representative span stations ($\eta = 0.150$, $\eta = 0.449$, $\eta = 0.681$, $\eta = 0.891$) and four angles of attack ($\alpha = 7.0$, $\alpha = 16.0$, $\alpha = 18.5$, $\alpha = 21.0$). In general, results computed on the two grids and using the two turbulence models agree well with each other and with experimental data at the lower angles of attack but discrepancies increase for the larger angles of attack and are more pronounced at the outboard stations. For example, at 16 degrees, differences begin to appear on the upper surface of the main wing element at the two outboard stations, which are seen to grow at 18.5 degrees with increased separation on the flap upper surface at the outer most station for the k-omega turbulence model runs. At 21 degrees, the models agree more closely with each other and with experimental data, as both models predict separation on the flap . For 16 degrees and above, the k-omega model on the VGRID mesh predicts the largest amount of separation at the outboard stations, while the Spalart-Allmaras model predicts the least amount, with the k-omega model on the ICEM grids falling in between these two.

Figures 22 through 23 depict a complete set of field velocity profiles In this case, the results obtained with both turbulence models on both grid systems are compared with experimental data, given the suitable fidelity of the current geometry and the availability of experimental data at this Reynolds number. In general, the agreement between models and with experimental data is reasonable for the 7 degree case. At 16 degrees, significant variations between the three sets of computations are observed, particularly at downstream and outboard profile locations. The k-omega results on the VGRID mesh show the largest velocity deficits and poorest agreement with experimental data in most cases, indicative of premature separation at 16 degrees. The Spalart-Allmaras results on the VGRID mesh are closest to the experimental results, but in all cases, certain flow features such as upstream generated wakes are either poorly captured or not captured at all. This points to the need for significant additional grid resolution in off-body regions of the computational domain in order to obtain better agreement, although the precise impact of resolving such flow features on overall force and moment prediction remains poorly understood.

VI. Case 2b - High Reynolds Number Alpha Sweep

Case 2b is similar to Case 2a with the exception that the Reynolds number is increased to 15.1 million. As previously, the same set of eight angles attack were specified for the workshop, and additional incidences were run near the maximum lift point as required in order to obtain a well resolved lift curve. Computations using both turbulence models were performed on both meshes for this case, leading to four sets of results to be compared with each other and with experimental data. The same meshes were used in Case 2b as Case 2a, since these meshes were designed to have the required $y^+ < 1$ normal wall resolution for the higher Reynolds number cases.

Figure 24 depicts the computed lift and drag coefficients as a function of angle of attack, as well as a drag polar and moment coefficient plot for all four runs. As previously, all of the results agree well in the linear region of the lift curve. Similarly, for the higher angles of attack, the Spalart-Allmaras results overpredict both lift and the $C_{L_{MAX}}$ location, while the k-omega results underpredict lift, although the $C_{L_{MAX}}$ point is well predicted on both meshes using this model. In particular, the k-omega results on the ICEM mesh agree relatively well with experimental results, including the shape of the curve in the stall region. It is notable that the Spalart-Allmaras results run on both mesh types agree very well with each other, while appreciable

differences in the k-omega results are observed between these two meshes.

Drag as a function on incidence is overpredicted in all four cases, with the k-omega results on the VGRID mesh producing the largest drag values, although the differences between the models and grids is slightly less than in the lower Reynolds number case (Case 2b). However, in terms of the drag polar, these results display the best post-stall agreement with experimental data, although the best agreement in the stall region of the drag polar is realized with the k-omega model on the ICEM mesh. The moment coefficients are overpredicted (in terms of absolute values) in the lower lift regions by all computations, with the best agreement in the stall region coming from the k-omega model on the ICEM mesh.

Computed surface pressure plots are given at the same four stations and incidences as in the previous case ($\eta = 0.150$, $\eta = 0.449$, $\eta = 0.681$, $\eta = 0.891$, and $\alpha = 7.0$, $\alpha = 16.0$, $\alpha = 18.5$, $\alpha = 21.0$) for all four runs in Figures 25 through 28. The trends are similar to those observed in the previous case, although it is notable that the Spalart-Allmaras results on both grids agree very well with each other over the entire range of conditions and locations shown. On the other hand, significant differences between the k-omega results on the two different meshes are observed at the higher angles of attack for the outermost span stations. These results do not necessarily imply that the k-omega turbulence model is more sensitive to grid resolution or topology. In the cases and regions where these discrepancies are observed, the flow exhibits appreciable regions of separation, as can be surmised from the flap pressure distributions at the outboard stations and at the higher angles of attack. It is well known that flows with significant regions of flow separation are more sensitive to grid resolution effects.[16] Since the Spalart-Allmaras results display little flow separation at these conditions, the observed discrepancies may be more related to the behavior of separated RANS flow simulations on meshes of moderate resolution, rather than specific differences in mesh sensitivities for these two turbulence models. Field velocity profiles are not plotted for this case since no experimental data was available at this Reynolds number.

VII. Surface Flow Visualization

Figure 29 depicts the surface "oil flow" (surface restricted streamlines) with a color contour plot of the surface skin friction coefficient, based on the solutions obtained on the VGRID mesh for Case 2b using the Spalart-Allmaras turbulence model. At the lower angle of attack, the flow is smooth and mostly attached across the entire wing span, although a side-of-body reverse flow region is seen even at these conditions, and smaller regions of flow separation behind the flap track fairings are observed. As the angle of attack is increased, these regions grow slightly in size, and at the stall point a massive separation region suddenly appears behind the second most outboard flap track fairing. This suggests that the stall mechanism is driven by the flap-track fairings and is corroborated by the workshop results showing that $C_{L_{MAX}}$ was grossly overpredicted for Case 1, when the slat brackets and flap track fairings are omitted.[3] The flow patterns shown in Figures 29 are similar to the experimental oil flow patterns obtained in the wind tunnel tests, as shown in Figure 1, although in the experimental data the large separation region occurs at a more inboard flap-track fairing location. However, the location of the flow separation region at stall observed in these computations is consistent with that obtained by a majority of the participants in the workshop results.

VIII. Conclusions

Two sets of results for the second high-lift prediction workshop (HLPW2) have been reported using the NSU3D unstructured mesh Reynolds-averaged Navier-Stokes solver. The two sets were performed independently and run on meshes constructed using different mesh generation software packages. Two different turbulence models were run on both sets of meshes in order to cross correlate the effects due to turbulence model variations with mesh sensitivity. In general, all the results agree relatively well for lower angles of attack, but differences are apparent near the maximum lift points. The Spalart-Allmaras results tend to overpredict the $C_{L_{MAX}}$ value and location, while the k-omega results provide better prediction of the $C_{L_{MAX}}$ location, although the $C_{L_{MAX}}$ values are generally underpredicted. The underprediction was more severe on the VGRID meshes, and the best overall predictions were obtained with the k-omega model using the ICEM meshes. In contrast to the differences observed with the k-omega model on the two different mesh types, the Spalart-Allmaras results on both sets of meshes agree well with each other. However, this may be due more to the increased presence of flow separation with the k-omega model rather than a fundamen-

tally larger sensitivity to mesh resolution of the model. The principal differences between these two mesh systems include more spanwise resolution in the ICEM meshes due to the use of mostly isotropic surface triangulations, along with a slower growth rate of cells in near well regions, leading to a larger number or prismatic elements in boundary layer regions. Results in terms of forces, moments, surface pressures, and field velocity profiles were consistent between the different turbulence models and meshes. Close inspection of these different aspects of the computational results could not conclusively show superior agreement for one model or the other with respect to detailed experimental data. Experimentally and computationally, the stall mechanism for this configuration is seen to be driven by the presence of flow separation behind the flap track fairings, although the specific flow separation patterns observed computationally in these results, as well in most other workshop results, are different than those observed experimentally.

Future work should investigate further the effects of grid resolution on the configuration that includes the slat brackets and flap track fairings. The effects of the pressure tube bundles in the more complex Case 3 geometry remain to be investigated, as well as the effects of transition. Finally, recent advances in solver robustness will be leveraged to accelerate convergence and increase robustness for difficult high lift cases such as those near stall.

IX. Acknowledgments

We are grateful for computer time provided on the NCAR-Wyoming Supercomputer and the University of Wyoming Advanced Research Computing Center.

References

[1]Rumsey, C. R., Long, M., Stuever, R. A., and Wayman, T. R., "Summary of the First AIAA High-Lift Prediction Workshop," AIAA Paper 2011-939 presented at the 49th AIAA Aerospace Sciences Meeting, Orlando FL.

[2]"Second AIAA High Lift Prediction Workshop." San Diego, CA. http://highliftpw.larc.nasa.gov.

[3]Rumsey, C. R. and Slotnick, J., "Overview and Summary of HiLiftPW-2," AIAA Paper 2014-xxx presented at the AIAA SciTech 2014 Conference, National Harbor, MD.

[4]Rudnick, R., "CFD Assessment for 3D high lift Flows in the European Project EUROLIFT," AIAA Paper 2003-3794.

[5]Hansen, H., Thiede, P., Moens, F., Rudnik, R., and Quest, J., "Overview About the European High Lift Research Programme EUROLIFT," AIAA Paper 2004-0767.

[6]Rudnick, Huber, K., and Melber-Wilkending, S., "EUROLIFT Test Case Description for the 2nd High Lift Prediction Workshop," AIAA Paper 2012-2924.

[7]Long, M. and Mavriplis, D. J., "NSU3D Results from the First AIAA CFD High-Lift Prediction Workshop," AIAA Paper 2011-863 presented at the 49th AIAA Aerospace Sciences Meeting.

[8]Mavriplis, D. J., Z.Yang, and Long, M., "Results using NSU3D for the First AIAA Aeroelastic Prediction Workshop," AIAA Paper 2013-0786, 51st AIAA Aerospace Sciences Meeting, Grapevine TX.

[9]Levy, D. W., Zickuhr, T., Vassberg, J., Agrawal, S., Wahls, R. A., Pirzadeh, S., and Hemsch, M. J., "Data Summary from the First AIAA Computational Fluid Dynamics Drag Prediction Workshop," *Journal of Aircraft*, Vol. 40, No. 5, 2003, pp. 875–882.

[10]Laflin, K., Klausmeyer, S. M., Zickuhr, T., Vassberg, J. C., Wahls, R. A., Morrison, J. H., Brodersen, O. P., Rakowitz, M. E., Tinoco, E. N., and Godard, J., "Data Summary from Second AIAA Computational Fluid Dynamics Drag Prediction Workshop," *Journal of Aircraft*, Vol. 42, No. 5, 2005, pp. 1165–1178.

[11]Vassberg, J. C., Tinoco, E. N., Mani, M., Brodersen, O. P., Eisfeld, B., Wahls, R. A., Morrison, J. H., Zickuhr, T., Laflin, K. R., and Mavriplis, D. J., "Abridged Summary of the Third AIAA Computational Fluid Dynamics Drag Prediction Workshop," *Journal of Aircraft*, Vol. 45, No. 3, 2008, pp. 781–798.

[12]Mavriplis, D. J. and Levy, D. W., "Transonic Drag Prediction using an Unstructured Multigrid Solver," *AIAA Journal of Aircraft*, Vol. 42, No. 4, 2003, pp. 887–893.

[13]Mavriplis, D. J., "Third Drag Prediction Workshop Results using the NSU3D Unstructured Mesh Solver," *AIAA Journal of Aircraft*, Vol. 45, No. 3, May 2008, pp. 750–761.

[14]Mavriplis, D. J. and Long, M., "NSU3D Results from the Fourth AIAA CFD Drag Prediction Workshop," AIAA Paper 2010-4364.

[15]Park, M., Laflin, K. R., Chaffin, M., Powell, N., and Levy, D. W., "CFL3D, FUN3D and NSU3D contributions to the fifth drag prediction workshop," AIAA Paper 2013-0050, 51st AIAA Aerospace Sciences Meeting, Grapevine TX.

[16]Mavriplis, D. J., Vassberg, J. C., Tinoco, E. N., Mani, M., Brodersen, O. P., Eisfeld, B., Wahls, R. A., Morrison, J. H., Zickuhr, T., and Levy, D., "Grid Quality and Resolution Issues from the Drag Prediction Workshop Series," AIAA Paper 2008-0930.

[17]Pirzadeh, S., "Three-Dimensional Unstructured Viscous Grids by the Advancing-Layers Method," *AIAA Journal*, Vol. 34, No. 1, 1996, pp. 43–49.

[18]"ANSYS ICEM CFD 14 User Manual," ANSYS Inc., Southpointe 275 Technology Drive, Canonsburg PA 15317.

[19]Mavriplis, D. J., "Grid Resolution Study of a Drag Prediction Workshop Configuration Using the NSU3D Unstructured Mesh Solver," AIAA-Paper 2005-4729.

[20]Mavriplis, D. J. and Venkatakrishnan, V., "A Unified Multigrid Solver for the Navier-Stokes Equations on Mixed Element Meshes," *International Journal for Computational Fluid Dynamics*, Vol. 8, 1997, pp. 247–263.

[21]Spalart, P. R. and Allmaras, S. R., "A One-equation Turbulence Model for Aerodynamic Flows," *La Recherche Aérospatiale*, Vol. 1, 1994, pp. 5–21.

[22]Wilcox, D. C., "Re-assessment of the scale-determining equation for advanced turbulence models," *AIAA Journal*, Vol. 26, 1988, pp. 1414–1421.

[23]Menter, F. R., "Two-Equation Eddy-Viscosity Turbulence Models for Engineering Applications," *AIAA Journal*, Vol. 32, No. 8, 1994, pp. 1598–1605.

[24]Mavriplis, D. J., "Multigrid Strategies for Viscous Flow Solvers on Anisotropic Unstructured Meshes," *Journal of Computational Physics*, Vol. 145, No. 1, Sept. 1998, pp. 141–165.

[25]Mavriplis, D. J. and Pirzadeh, S., "Large-Scale Parallel Unstructured Mesh Computations for 3D High-Lift Analysis," *AIAA Journal of Aircraft*, Vol. 36, No. 6, Dec. 1999, pp. 987–998.

[26]Mavriplis, D. J. and Mani, K., "Unstructured Mesh Solution Techniques using the NSU3D Solver," AIAA Paper 2014-xxx, AIAA Scitech 2014 Conference, National Harbor, MD.

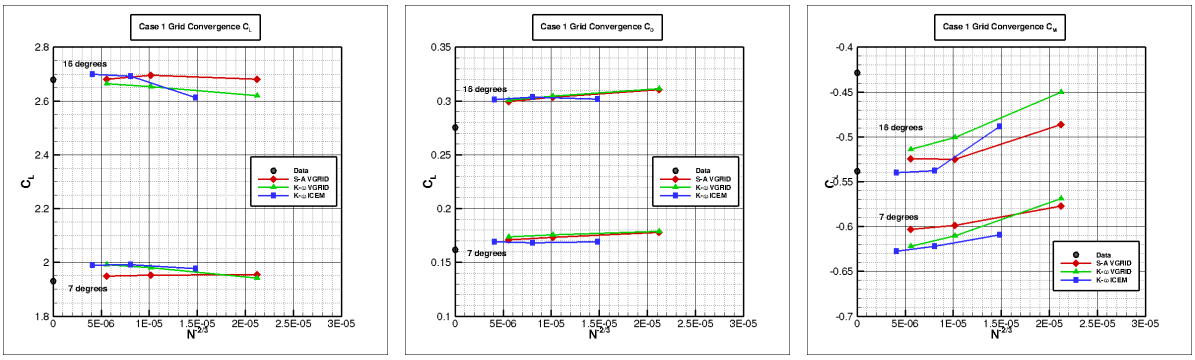

Figure 10. Grid convergence for both turbulence models on VGRID generated meshes and for k-omega model on ICEM generated meshes for Case 1

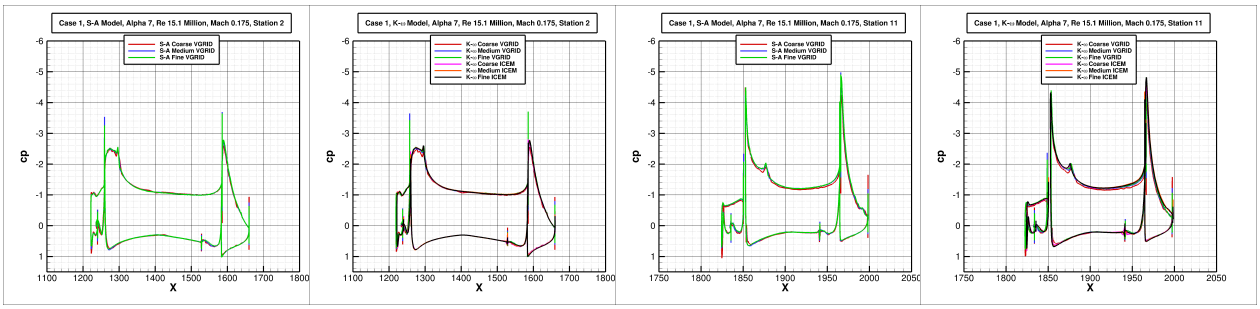

Figure 11. Variation of computed surface pressure coefficients with grid resolution for Case 1 at 7 degrees incidence for both turbulence models at second inboard and outermost span stations

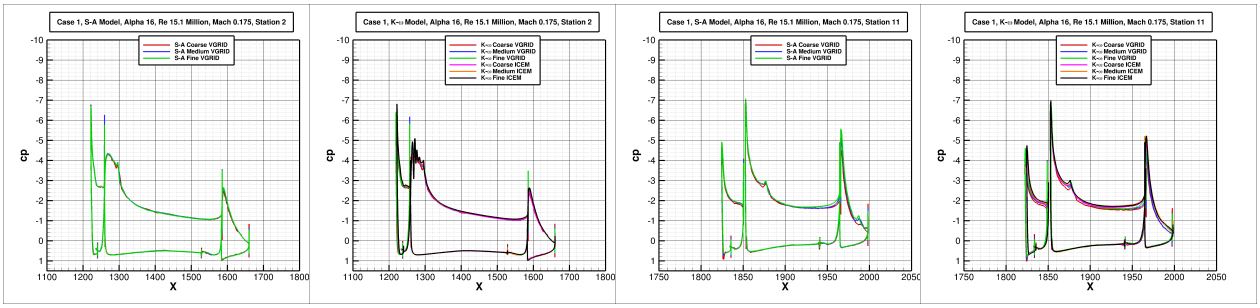

Figure 12. Variation of computed surface pressure coefficients with grid resolution for Case 1 at 16 degrees incidence for both turbulence models at second inboard and outermost span stations

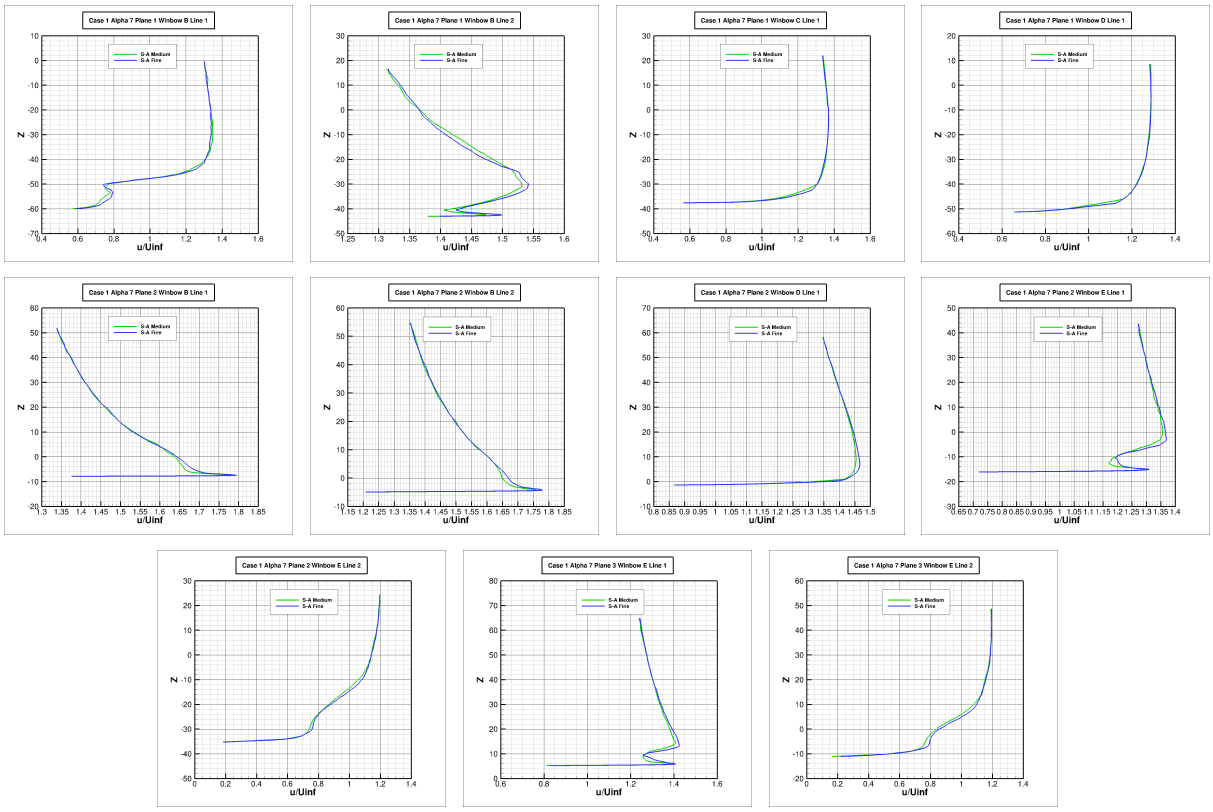

Figure 13. Effect of grid resolution on velocity profiles for Case 1 at 7 degrees using Spalart-Allmaras turbulence model on VGRID generated meshes

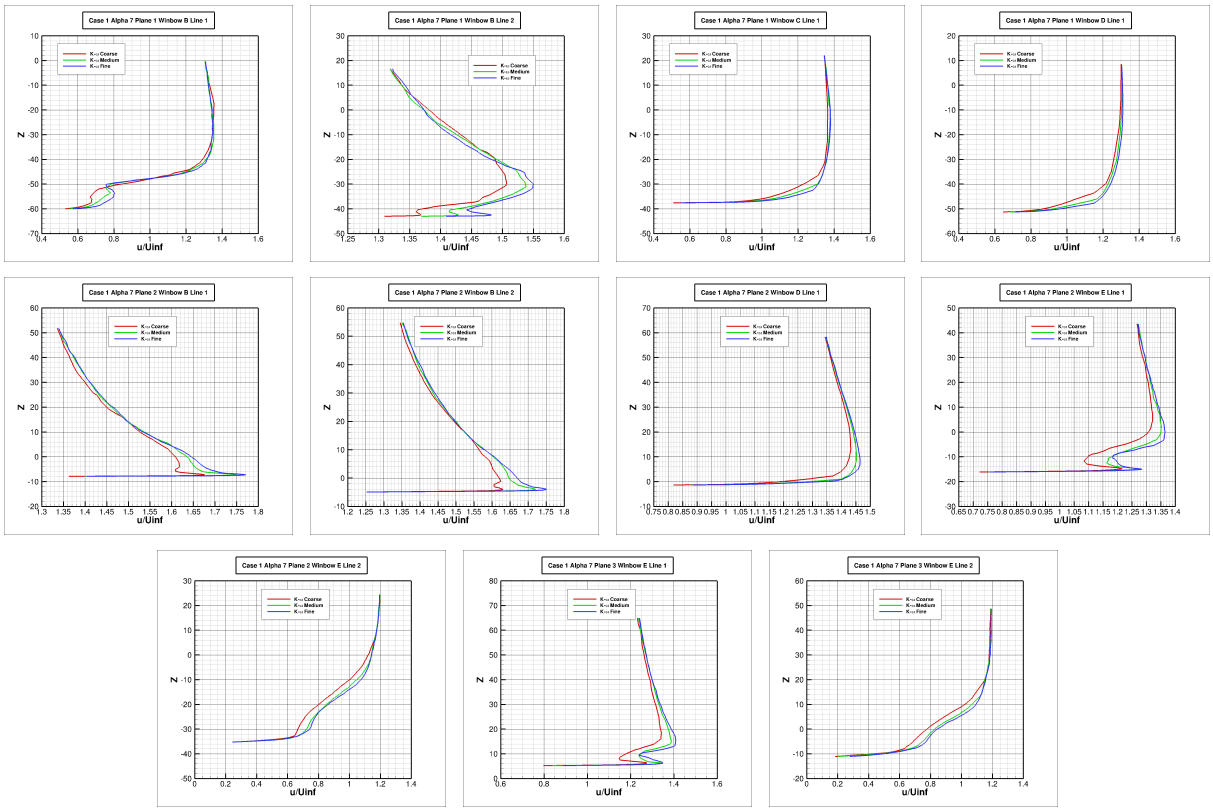

Figure 14. Effect of grid resolution on velocity profiles for Case 1 at 7 degrees using k-omega turbulence model on VGRID generated meshes

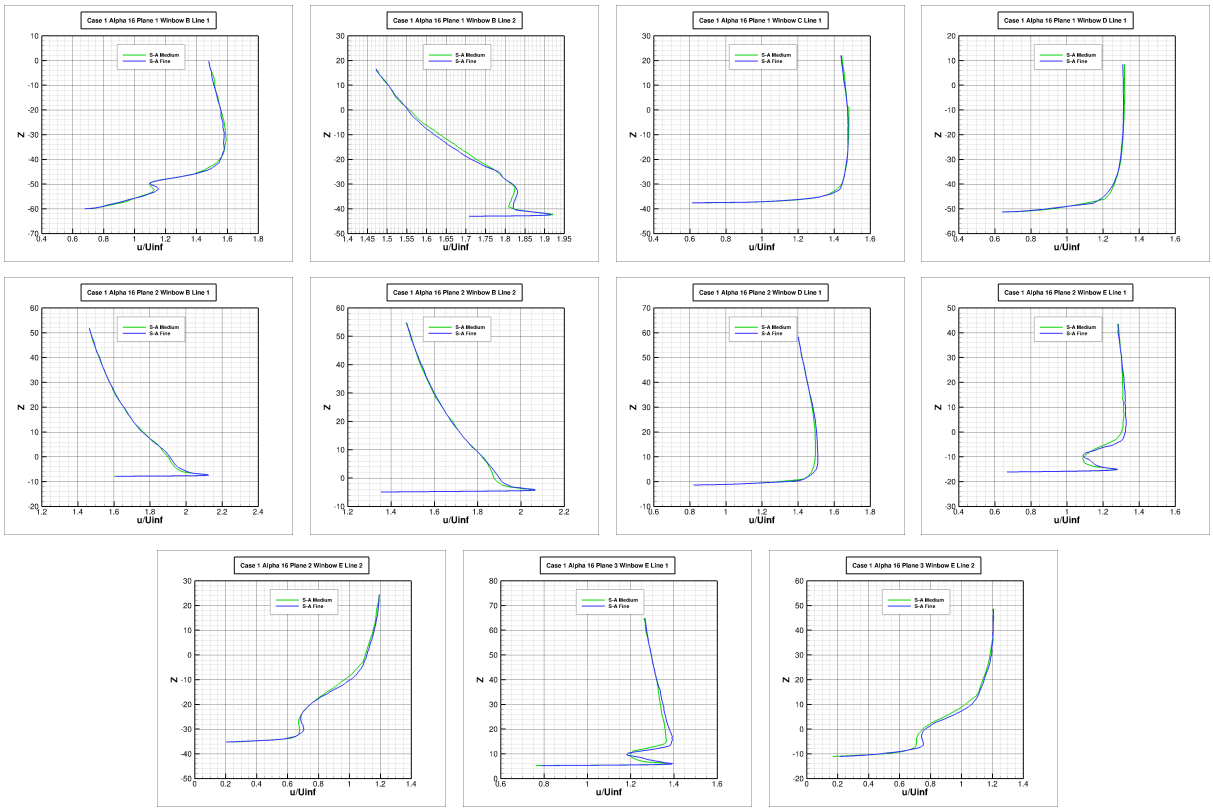

Figure 15. Effect of grid resolution on velocity profiles for Case 1 at 16 degrees using Spalart-Allmaras turbulence model on VGRID generated meshes

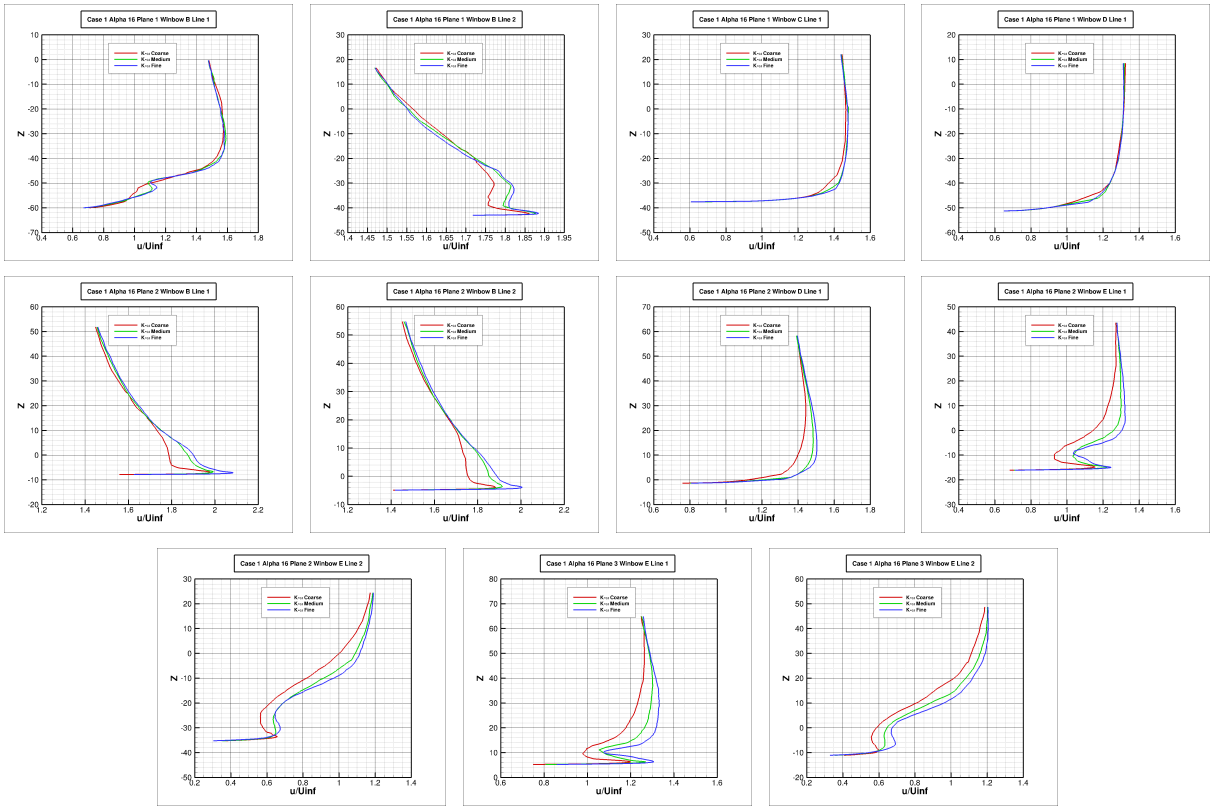

Figure 16. Effect of grid resolution on velocity profiles for Case 1 at 16 degrees using k-omega turbulence model on VGRID generated meshes

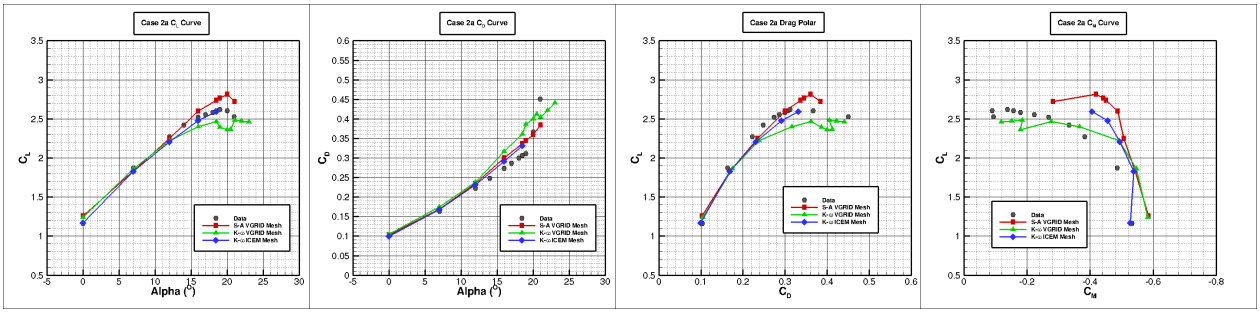

Figure 17. Lift, drag and moment predictions for both turbulence models on both grid types for low Reynolds number Case 2a

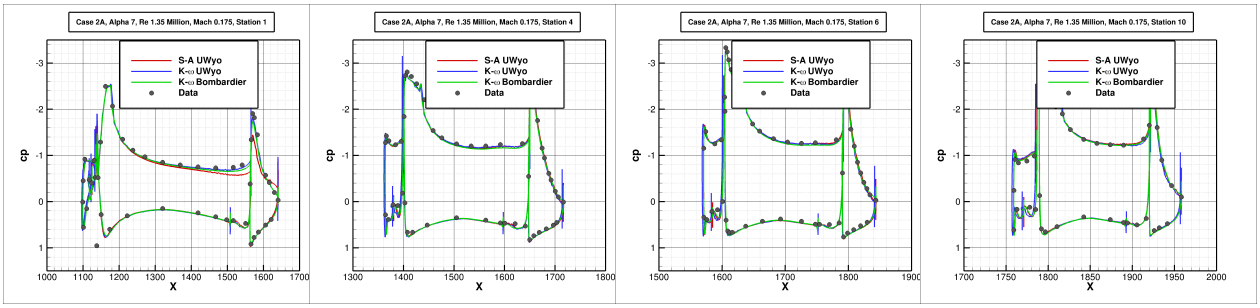

Figure 18. Computed surface pressure coefficients for Case 2a at 7 degrees incidence

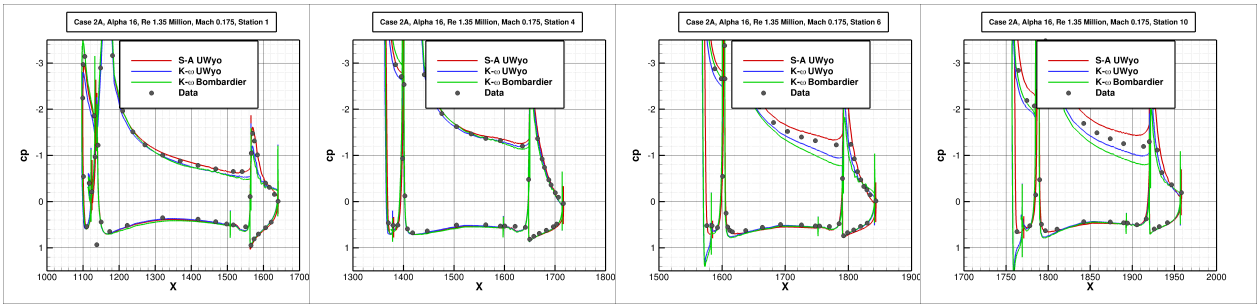

Figure 19. Computed surface pressure coefficients at for Case 2a at 16 degrees incidence

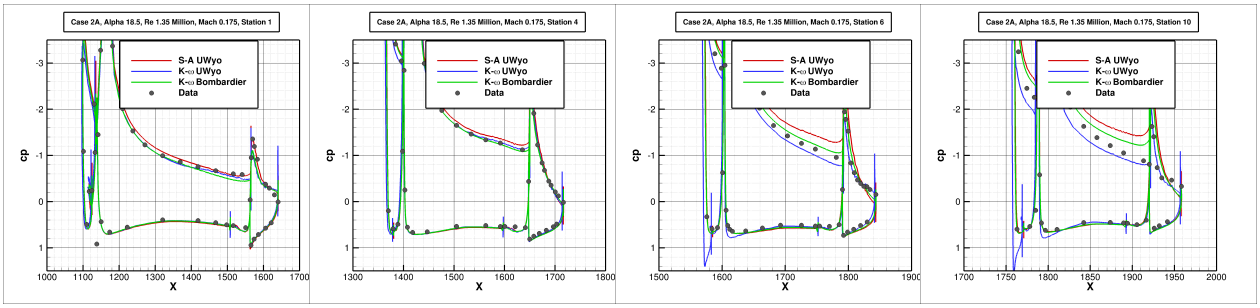

Figure 20. Computed surface pressure coefficients at for Case 2a at 18.5 degrees incidence

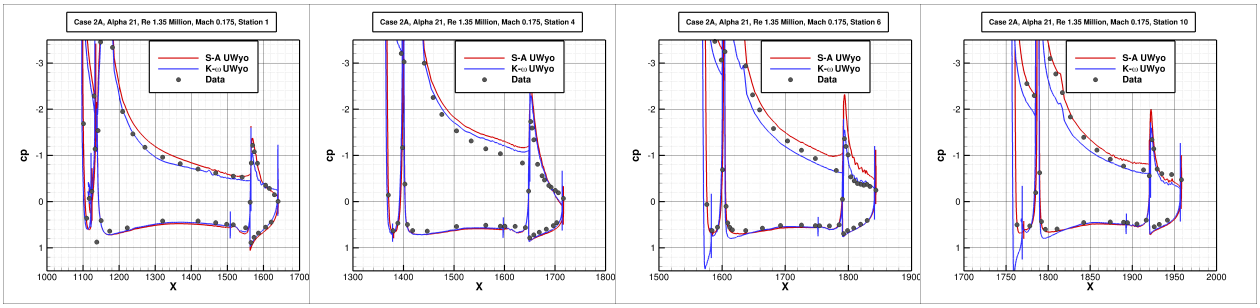

Figure 21. Computed surface pressure coefficients at for Case 2a at 21 degrees incidence

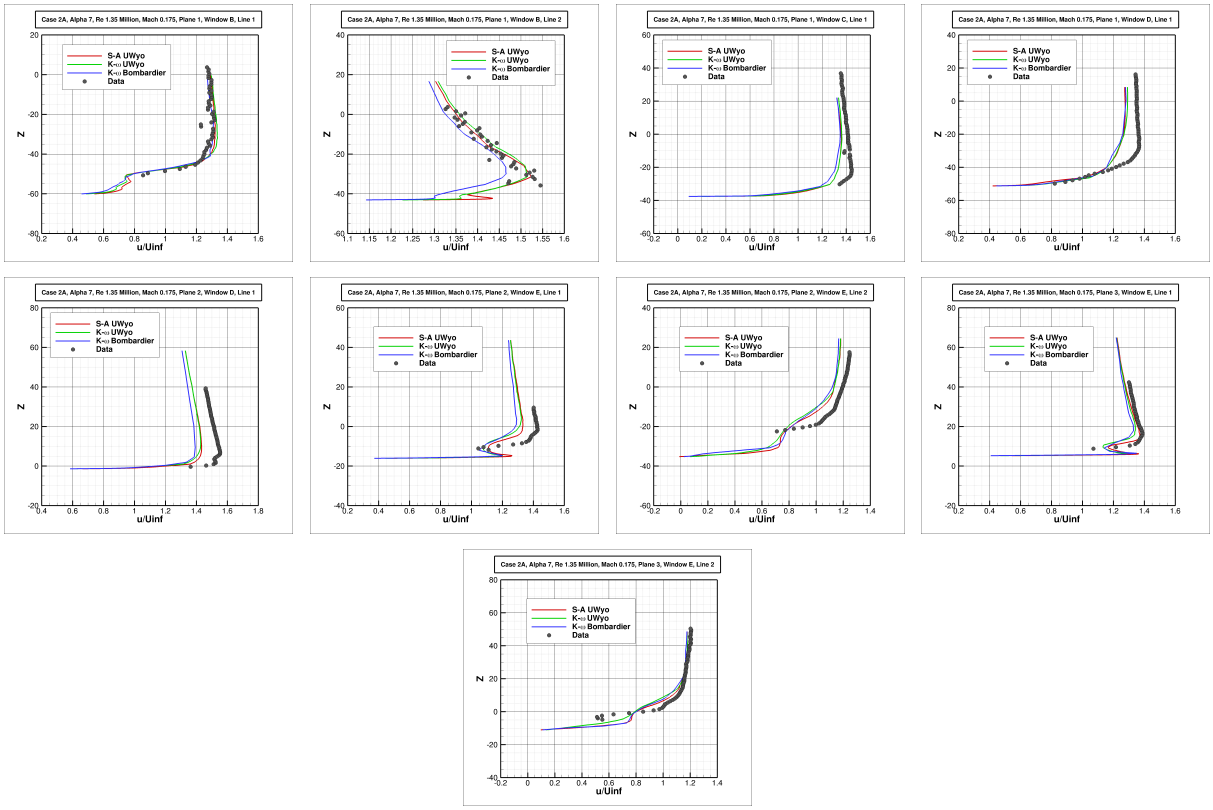

Figure 22. Computed velocity profiles at 7 degrees incidence for Case 2a using two turbulence models and both grids compared with experimental data

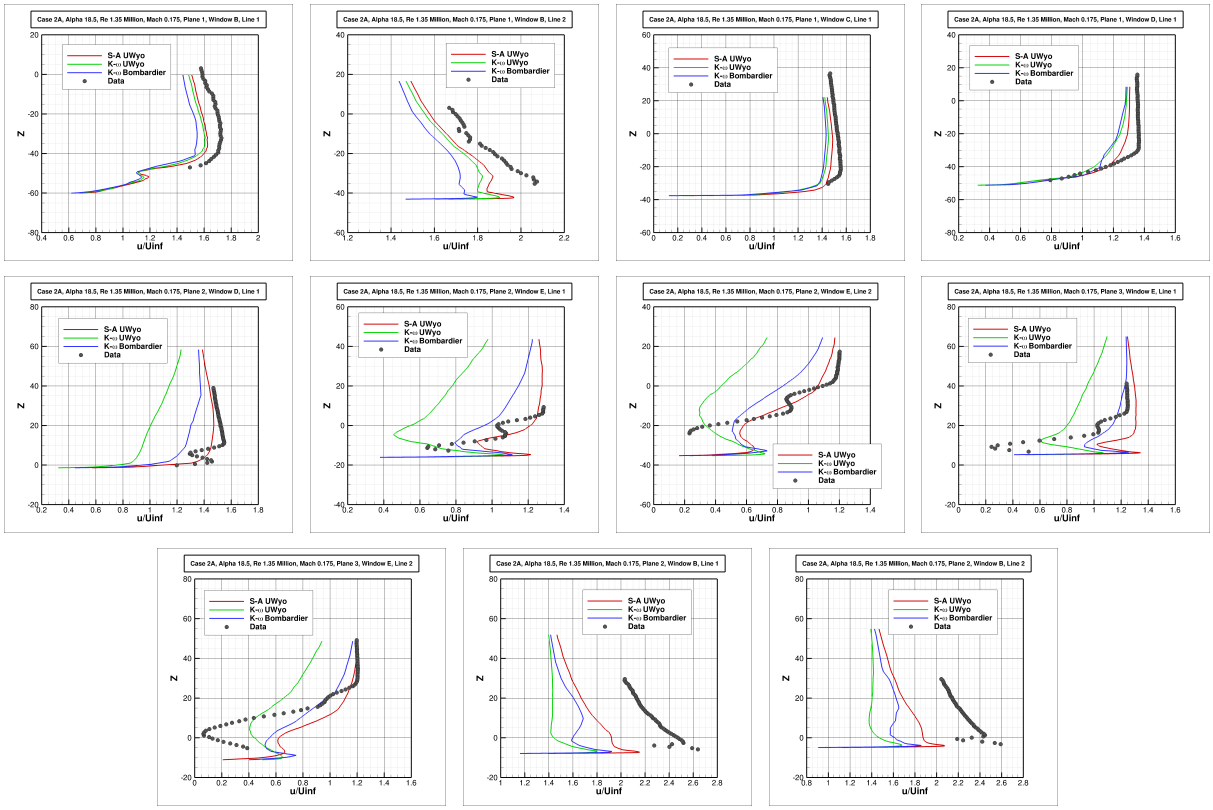

Figure 23. Computed velocity profiles at 18.5 degrees incidence for Case 2a using two turbulence models and both grids compared with experimental data

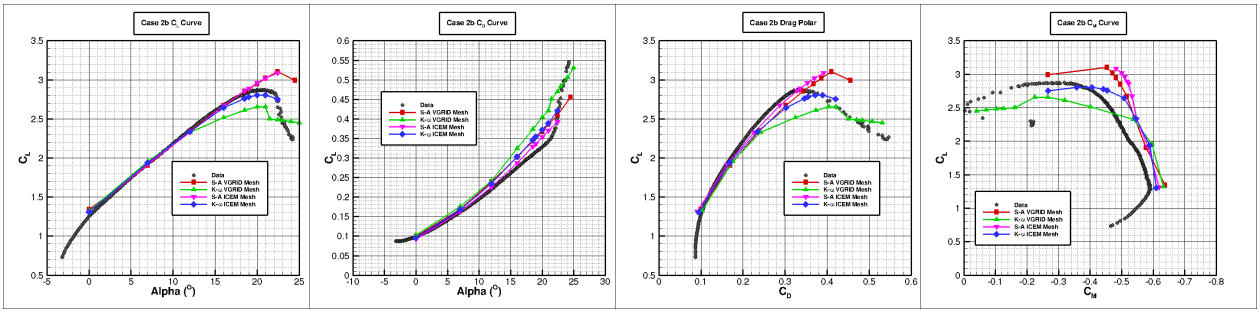

Figure 24. Lift, drag and moment predictions for both turbulence models on both grid types for high Reynolds number Case 2b

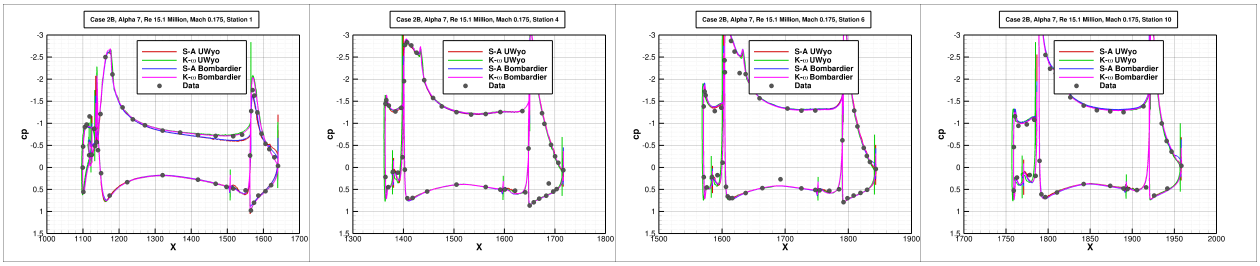

Figure 25. Computed surface pressure coefficients for Case 2b at 7 degrees incidence

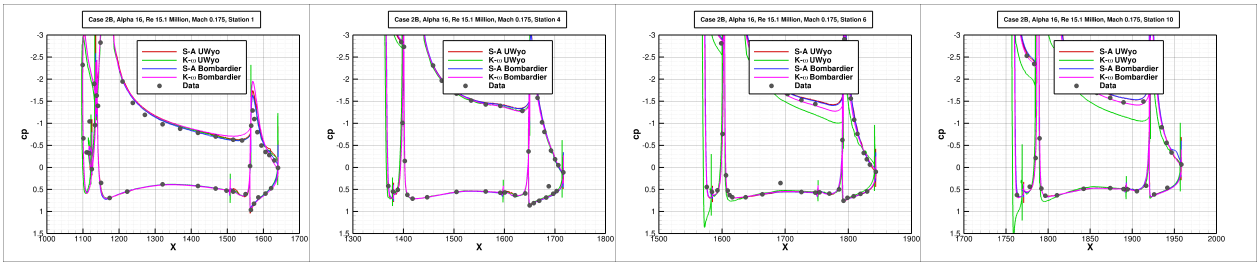

Figure 26. Computed surface pressure coefficients for Case 2b at 16 degrees incidence

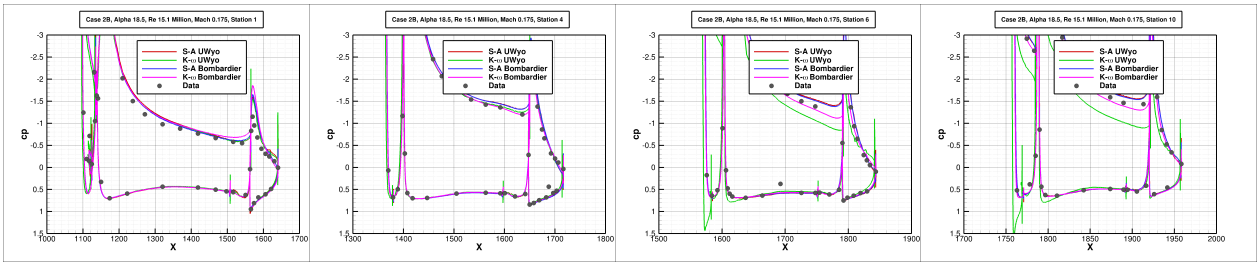

Figure 27. Computed surface pressure coefficients for Case 2b at 18.5 degrees incidence

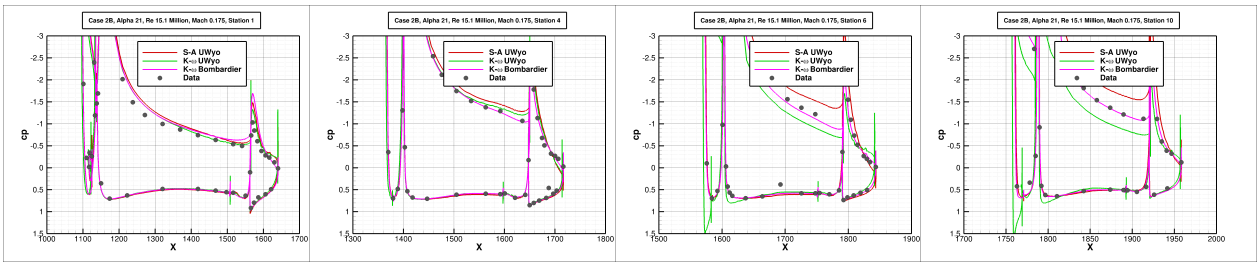

Figure 28. Computed surface pressure coefficients for Case 2b at 21 degrees incidence

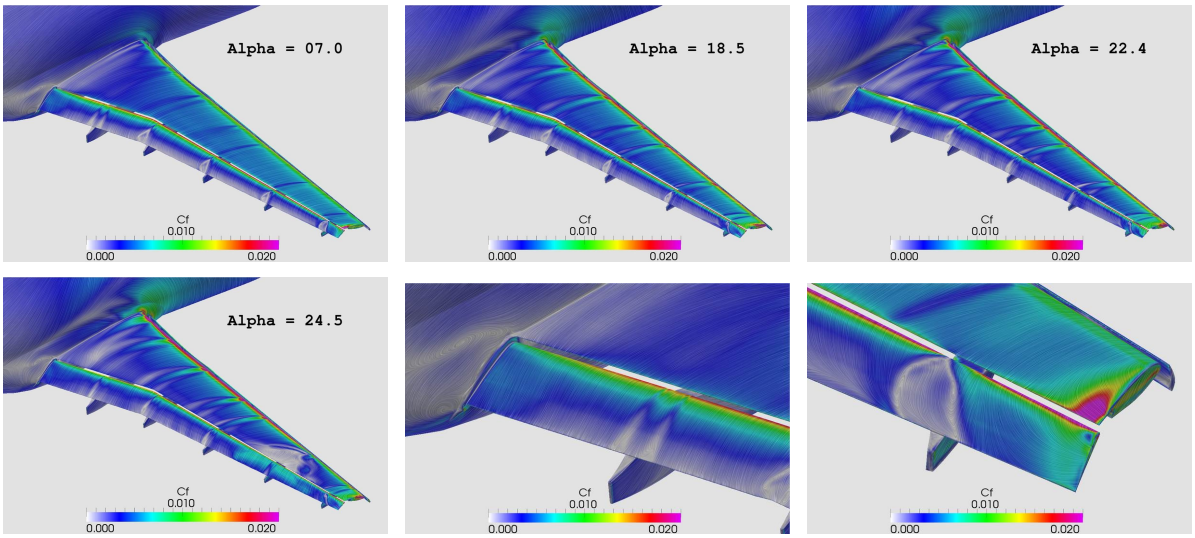

Figure 29. Surface skin friction and oil flow patterns for Case 2a using Spalart-Allamaras turbulence model illustrating stall mechanism